Published in final edited form as:
Chemphyschem. 2014 December 15; 15(18): 4100–4107. doi:10.1002/cphc.201402607.

In Situ and Ex Situ Low-Field NMR Spectroscopy and MRI Endowed by SABRE Hyperpolarization**

Danila A. Barskiy[a], **Kirill V. Kovtunov**[a], **Igor V. Koptyug**[a,*], **Ping He**[b], **Kirsten A. Groome**[b], **Quinn A. Best**[b], **Fan Shi**[b], **Boyd M. Goodson**[b], **Roman V. Shchepin**[c], **Milton L. Truong**[c], **Aaron M. Coffey**[c], **Kevin W. Waddell**[c], and **Eduard Y. Chekmenev**[c,*]

[a]Laboratory of Magnetic Resonance Microimaging, International Tomography Center, SB RAS, 3 A Institutskaya St., Novosibirsk 630090 (Russia)

[b]Department of Chemistry and Biochemistry, Southern Illinois University, Materials Technology Center, Carbondale, Illinois, 62901 (USA)

[c]Institute of Imaging Science, Department of Radiology, Department of Biomedical Engineering, Department of Physics and Astronomy and Department of Biochemistry, Vanderbilt University, 1161 21 st Ave South AA-1107, Nashville, Tennessee, 37232-2310 (USA)

Abstract

By using 5.75 and 47.5 mT nuclear magnetic resonance (NMR) spectroscopy, up to 10^5-fold sensitivity enhancement through signal amplification by reversible exchange (SABRE) was enabled, and subsecond temporal resolution was used to monitor an exchange reaction that resulted in the buildup and decay of hyperpolarized species after parahydrogen bubbling. We demonstrated the high-resolution low-field proton magnetic resonance imaging (MRI) of pyridine in a 47.5 mT magnetic field endowed by SABRE. Molecular imaging (i.e. imaging of dilute hyperpolarized substances rather than the bulk medium) was conducted in two regimes: in situ real-time MRI of the reaction mixture (in which pyridine was hyperpolarized), and ex situ MRI (in which hyperpolarization decays) of the liquid hyperpolarized product. Low-field (milli-Tesla range, e.g. 5.75 and 47.5 mT used in this study) parahydrogen-enhanced NMR and MRI, which are free from the limitations of high-field magnetic resonance (including susceptibility-induced gradients of the static magnetic field at phase interfaces), potentially enables new imaging applications as well as differentiation of hyperpolarized chemical species on demand by exploiting spin manipulations with static and alternating magnetic fields.

Keywords

hyperpolarization; iridium; NMR spectroscopy; molecular imaging; SABRE

**SABRE=Signal Amplification by Reversible Exchange

Novosibirsk State University, 2 Pirogova St., Novosibirsk 630090 (Russia), koptyug@tomo.nsc.ru.

Supporting Information for this article is available on the WWW under http://dx.doi.org/10.1002/cphc.201402607.

1. Introduction

Nuclear magnetic resonance (NMR) spectroscopy and magnetic resonance imaging (MRI) are among the most powerful analytical tools for noninvasive studies of structure and dynamics at macroscopic, microscopic, and molecular scales.[1] However, owing to low nuclear spin polarization (*P*), defined as the normalized population difference between Zeeman energy levels, NMR and MRI are collectively known as relatively low-sensitivity techniques.[2] Whereas *P* increases linearly with the applied static magnetic field, it remains at a relatively low level even if powerful magnets are used. For example, *P* of proton spins is only 3×10^{-5} at 9.4 T under ambient conditions. Moreover, high-field NMR and MRI have several fundamental challenges preventing their widespread in situ use in the chemical industry. First, high-field NMR and MRI can generally encompass only relatively small- to medium-sized objects (centimeter to decimeter scale, and most MRI scanners have a bore/gap size of 60 cm or less) and carry high instrumentation and operational costs. Second, the magnetic susceptibility differences may be rather significant at phase interfaces (e.g. gas–liquid, solid–liquid), which makes their imaging at high static (B_0) and alternating (B_1) fields extremely challenging due to arising imaging artifacts.[3]

Low-field NMR/MRI obviates the above limitations of high-field NMR/MRI. Less costly magnets can be constructed for operation below 0.1 T by using permanent and resistive magnet technologies.[4] Furthermore, low resonance frequencies are significantly less prone to imaging artifacts at phase interfaces primarily due to decreased magnetic field susceptibility-induced gradients. The main general drawback of low-field MRI is the inherently low signal-to-noise ratio (SNR) due to a low nuclear spin polarization at equilibrium, which scales linearly with the applied magnetic field. For example, the proton nuclear spin polarization at 6 mT field is only 2×10^{-8}. [5] However, the sensitivity barrier of low-field MRI/NMR can be overcome through artificial temporary manipulation of nuclear spin polarization by using a range of techniques collectively known as hyperpolarization, which enhance nuclear spin polarization (and the resulting signal and SNR). Increasing nuclear spin polarization to the order of unity at such low magnetic fields, therefore, increases NMR sensitivity by more than eight orders of magnitude.[6] Furthermore, the recent advent of more sophisticated low-field MRI detectors [i.e. radiofrequency (RF) coils] not only achieves SNRs that are comparable to those of high-field MRI detectors of hyperpolarized (HP) media/contrast agents but potentially can make HP MRI more sensitive at low magnetic fields than at high magnetic fields.[7] These prospects of HP low-field MRI potentially enable new applications including molecular imaging in vivo and imaging of chemical processes.

Various techniques—for example, spin-exchange optical pumping (SEOP) of noble gases,[8] dynamic nuclear polarization (DNP),[9] parahydrogen-induced polarization (PHIP)[10] and signal amplification by reversible exchange (SABRE)[11]—can be used to prepare HP contrast agents. Parahydrogen-based approaches (PHIP and SABRE) relying on chemical reaction or exchange with parahydrogen (p-H_2) are promising candidates for production of HP contrast agents, because they are inexpensive, rapidly achieve the hyperpolarized state, and can be scaled to potentially meet any specific requirements. Because PHIP/SABRE hyperpolarization is achieved by “unlocking” the p-H_2 singlet state by reacting or

exchanging *p*-H_2, it becomes possible to detect intermediates or low-concentration products while generating hyperpolarization continuously with replenished *p*-H_2 gas.

SABRE hyperpolarization is based on the reversible interaction of a polarizable substrate molecule with *p*-H_2 on a metal complex in solution.[11a, 12] The fundamental difference between SABRE and PHIP is that SABRE does not modify the molecular structure of the contrast agent during hyperpolarization build-up. Moreover, heterogeneous (HET) SABRE was recently demonstrated with a metal complex immobilized on the surface of polymer beads,[13] which enabled the separation of a liquid substrate from a heterogeneous solid catalyst. Although the demonstrated HET SABRE enhancements are relatively small, potential future improvements can lead to the preparation of pure HP liquids by SABRE for biomedical applications. Recent progress in the development of SABRE catalysts in aqueous media is very encouraging and should facilitate the use of SABRE HP contrast agents in living organisms.[14]

Originally, the SABRE effect was limited to *p*-H_2/substrate chemical exchange at low magnetic field of a few milli-Tesla for which coherent *J* coupling mediated polarization transfer should be efficient.[15] However, SABRE was recently shown to be feasible at high magnetic fields, consistent with an incoherent mechanism of polarization transfer.[16] High-field in situ SABRE (although relatively inefficient for substrate hyperpolarization if compared to conventional low-field SABRE) at 9.4 T revealed several additional HP species including orthohydrogen (*o*-H_2) and a Ir–dihydride complex; the presence of the Ir complex has to be accounted for in low-field NMR where chemical shift dispersion is limited.

Building on our demonstration of in situ PHIP[17] spectroscopic detection and ex situ SABRE[18] MRI detection and the recent work of others,[14b, 19] herein we present high-resolution MRI imaging and spectroscopy of a SABRE chemical-exchange reaction by using a combination of in situ and ex situ low-field NMR/MRI approaches. Ex situ NMR spectra and MRI images of a liquid solution after exchange with *p*-H_2 were obtained at 47.5 mT with sub-millimeter in-plane spatial resolution (pixel size 125 × 125 μm^2) and a large imaging matrix of up to 512 × 512. Furthermore, in situ low-field NMR at 5.75 mT and in situ MRI and NMR at 47.5 mT were also employed for detection of the substrate (i.e. pyridine) and intermediates (i.e. iridium dihydride) of hydrogen exchange during the process of continuous *p*-H_2 bubbling though the solution. The latter would be especially challenging by high-field MR techniques due to susceptibility-induced magnetic field gradients at the phase interfaces.

2. Results and Discussion

2.1. In Situ and Ex Situ Studies at 47.5mT

SABRE hyperpolarization was achieved by bubbling *p*-H_2 gas through a solution of pyridine (Py) in [D_4]MeOH inside 5.75 and 47.5 mT magnets (Figure 1). Whereas SABRE at about 6 mT field has been shown to be very efficient for substrates such as Py [more than 1% nuclear spin polarization achieved corresponding to a sensitivity enhancement (ε) of 5×10^5 and 6×10^4 at 5.75 and 47.5 mT, respectively],[11a, 12] hyperpolarization at 47.5 mT largely relies on the high-field SABRE effect, which significantly enhances not only proton

polarization of Py but also the proton nuclear spin polarization of Ir–dihydride and *o*-H_2.[16] As a result, an in situ proton NMR spectrum acquired during *p*-H_2 bubbling at 47.5 mT has two distinctive NMR resonances detected at 47.5 mT (Figure 2 a). On the basis of the previous high-field SABRE in situ NMR spectroscopy studies at 9.4 T,[16] these two resonances are assigned to HP Py and Ir–dihydride due to their chemical shift difference of 31.5 ppm, which corresponds to a frequency separation of 64 Hz at 47.5 mT (2.02 MHz ^{1}H frequency). Notably, HP signals from the Py protons ($\delta \approx 8$–8.5 ppm) and HP *o*-H_2 ($\delta \approx 4.5$ ppm) cannot be distinguished due to a relatively broad NMR line with a full width at half height (FWHH) of about 20 Hz and a chemical shift difference of only 9–10 Hz. Therefore, it is likely that the NMR resonance assigned to Py (Figure 2 a) has some signal contribution from HP *o*-H_2, but this contribution is expected to be smaller than the signal contribution from Ir–dihydride.[16] Figure 2 b provides a signal reference spectrum from neat Py (12.4 м) that further confirms that the resonance drawn in grayshade in the spectrum of Figure 2 a is indeed a signature of five HP protons of Py. Remarkably, the spectrum in Figure 2 a was acquired during *p*-H_2 bubbling through the Py solution, that is, in the presence of susceptibility-induced magnetic field gradients. These gradients significantly broaden NMR resonances (to hundreds of hertz) at high magnetic field, which makes the detection experimentally challenging during on-going heterogeneous reactions under continuous supply of *p*-H_2 gas, the source of hyperpolarization. These results clearly demonstrate the advantage of low-field in situ NMR detection, which can be potentially scaled to large sample volumes. Notably, the large chemical shift difference between the protons of Ir–dihydride and Py/*o*-H_2 makes direct spectroscopic chemical differentiation at 47.5 mT possible; indeed, the spectrum comprises a rare example, in that resonances from different species at low field may be distinguished by chemical shift alone. Moreover, if the experiment were to be repeated wherein the Py substrate had been deuterated (thereby suppressing the HP Py signal), it would also become possible to perform NMR detection and differentiation of Ir–dihydride and *o*-H_2, which are the intermediates/byproducts of hydrogen exchange.

Although in situ SABRE detection at low magnetic field was already demonstrated by Hövener et al.,[14b, 19] the entire proton NMR resonance line was assigned to HP pyridine, as the formation of HP *o*-H_2 and Ir–dihydride were not reported at that time. Nevertheless, to perform analytical measurements (i.e. drug screening[20] and nanomolar substrate detection[21]) by using SABRE the presence of all major HP intermediate species must be quantitatively determined. For example, Figure 2 a shows two signals with a relative intensity ratio of (6.2 ± 0.3).

The ex situ detection of HP Py was performed when *p*-H_2 bubbling was performed and stopped at 5.75 mT, and then the sample was transferred for NMR detection inside a 47.5 mT magnet (Figure 3 b). The approximately 8 s long transfer time resulted in expected rapid depolarization of the intermediates/byproducts of Ir–dihydride and *o*-H_2 due to their relatively short spin lattice relaxation time (T_1) values of about 3 s.[16] Furthermore, the hyperpolarization of Py at 5.75 mT was approximately two orders of magnitude greater than that at 47.5 mT, as seen in Figure 3 a, b, and accounting for the HP Py polarization decay [$T_1 = (7.7 \pm 0.1)$ s] shown in Figure 3 c. This stark difference in HP signal strength is

expected, because SABRE hyperpolarization mechanisms at low (≈6 mT) and high fields are different.[15–16, 22] As a result, it is concluded that most of the ex situ signal (Figure 3 b) originates from HP Py rather than other HP species. The average percent polarization per proton of HP Py (Figure 3 b) was found to be (1.6 ± 0.16) % (see the Experimental Section) at the time of ex situ detection, which corresponds to an enhancement factor $\varepsilon = (1 \pm 0.1) \times 10^5$. Actual Py proton hyperpolarization at the time of its creation at 5.75 mT prior to sample transfer is expected to be greater than the enhancement derived from the signal observed at 47.5 mT due to the following factors: 1) potential overlap between adsorptive–emissive ^{1}H signals of the *ortho*, *meta*, and *para* protons of Py, and 2) T_1 relaxation during the time of sample transfer (≈8 s). Thus, whereas the ex situ detection of SABRE at 47.5 mT enables significantly better hyperpolarized molecules to be generated, in situ detection offers the advantage of additional chemical information, i.e., reporting on multiple HP species.

In situ 2D MRI (Figure 3 d) enabled the recording of molecular images with 0.75 × 0.75 mm^2 in-plane spatial and 4.5 min temporal resolution, whereas the higher polarization achieved for ex situ 2D MRI (Figure 3 e) resulted in a better in-plane spatial resolution of 0.125 × 0.125 mm^2 and ≤7.7 s temporal resolution. Despite the fact that the available signals for the in situ and ex situ experiments differ by more than two orders of magnitude, it was possible to record MRI images with good spatial resolution (measured as the pixel size) in both cases. This is in part explained by a larger excitation RF pulse tipping angle used for in situ MRI and the use of signal averaging, which is made feasible by the presence of constantly renewable polarization that quickly accumulates.[19] Note that in situ signal buildup was measured at 5.75 mT, which yielded a time constant of only (7.4 ± 0.3) s. This ability to perform multiple identical scans during *p*-H_2 delivery is a clear benefit of in situ imaging, which can be further explored to improve spatial resolution at the expense of temporal resolution. In situ imaging of the SABRE process is more advantageous than previously demonstrated field cycling detection of renewable SABRE hyperpolarization,[19] for which the field is swept between two modes corresponding to hyperpolarization buildup at about 6 mT followed by MRI at Earth field in the same setup without sample transfer. However, this method allowed only one line of the MRI *k*-space to be recorded every 8 s [i.e. repetition time (TR)], whereas the in situ method presented herein allowed for a TR of 0.2 s. Moreover, the achieved spatial resolution (0.75 × 0.75 mm^2 in-plane pixel size) was significantly better than that demonstrated previously (2 × 2 mm^2 in-plane pixel size[19]) by using samples of approximately the same volume (≈ 3 mL), Py concentration, and dimensions.

In situ 2D MRI can potentially reveal additional dynamic processes. For example, the bright spot seen in the in situ image (Figure 3 d, top) is clearly missing in the ex situ (Figure 3 e, top) image. This is likely explained by the process of *p*-H_2 entering the solution at the bottom of the 10 mm NMR tube through a tube with an outer diameter (OD) of 1.6 mm (seen as the hole in the corresponding MRI images). The fresh *p*-H_2 that is introduced is likely rapidly exchanged on the Ir–dihydride complex, which results in greater MRI intensities in the image pixels of the active reaction zone of the hyperpolarization buildup. The in situ MRI image recorded along the length of the NMR tube (Figure 3 d, bottom) supports this hypothesis that the active zone is indeed limited predominantly to the lower

section of the NMR tube immediately at the exit of the 1.6 mm OD tubing used for p-H_2 delivery. Moreover, this observation implies that SABRE hyperpolarization in a 10 mm NMR tube may have been significantly constrained by availability of p-H_2 as a source of hyperpolarization, which leads to a relatively low P_H. Indeed, $P_H = (1.6 \pm 0.16)$ % was observed in a 5 mm medium-walled NMR tube filled with about 0.75 mL of solution compared to $P_H = (0.2 \pm 0.02)$ % that was observed in a 10 mm NMR tube filled with about 3 mL of solution; this is in qualitative agreement with the in situ imaging studies. Notably, whereas our previous study (focusing primarily on enabling instrumentation technologies and imaging aspects of ^1H and ^{13}C hyperpolarized contrast media)[18] reported ex situ MRI images, this work additionally reports on the feasibility of in situ imaging of a real-time chemical reaction. Unlike our recent work[18] and the work of Hövener et al.,[19] the in situ MRI shown herein (Figure 3 d) takes snapshots in real time instead of delays of around 8 s[18] or 4 s.[19] This is a clear advantage, because some species (e.g. HP orthohydrogen and HP Ir–dihydride) are short lived and because of the convenience of data acquisition.

The in situ images presented correspond to the distribution of HP Py as well as to dissolved HP o-H_2 gas and the Ir–dihydride complex in the liquid phase during continuous bubbling of p-H_2 through the NMR tube containing the reaction mixture. As already discussed above, if the Py substrate were replaced by deuterated Py, in principle it should be possible to image only intermediates/byproducts: HP o-H_2 and Ir–dihydride. Upon performing the hyperpolarization at 5.75 mT and then transferring the sample to 47.5 mT for ex situ detection, the signal was mainly from HP Py (see above).

This low-field detection approach—enabled by the use of p-H_2 as a source of hyperpolarization and an exchangeable substrate as a molecular contrast agent—can be potentially extended to visualize industrial-scale processes in chemical reactors involving gas to liquid transfer, for example, gas purification, oxidation, chlorination, hydrogenation, and hydroformylation, in which p-H_2 can be potentially added to the gas stream (instead of normal H_2) while the substrate is present in trace quantities in solution.[23] In situ and ex situ MR molecular images presented in this study were obtained with <2% hyperpolarized agent; achieving higher levels of hyperpolarization in combination with improved pulse sequences (including 3D) and compressed sensing[24] may provide significantly better spatial and temporal resolution.

The low-field NMR/MRI setup presented is relatively simple, does not require cryogenically cooled superconducting magnets, and may utilize home-built electromagnets and RF probes.[7a] Relatively low concentrations of HP compounds such as Py are sufficient for low-field molecular MRI. SABRE already offers a range of substrates that can be hyperpolarized, including biocompatible molecules and metabolites,[25] and the list is likely to expand. Whereas the initially demonstrated signal enhancements with heterogeneous SABRE[13] and SABRE in water[14a, c] were relatively low, they can potentially enable SABRE imaging and spectroscopy in vivo. Moreover, manipulations with alternating magnetic fields (B_1) such as RF pulse sequences[26] and continuous RF irradiation[27] might provide efficient means for storage of hyperpolarization in the long-lived nuclear spin states, and therefore, the lifetime of hyperpolarization of contrast agents could be significantly

extended. This practice could further increase the range of potential in vivo and industrial applications, and the processes under study might be tracked on the timescale of minutes.[28]

2.2. In Situ Studies at 5.75 mT

The feasibility of time-resolved spectroscopy was investigated at a significantly lower magnetic field of 5.75 mT (compared to 47.5 mT), which was readily generated by a home-built electromagnet and a constant-current power supply. Figure 4 a demonstrates the single-scan HP NMR spectrum from the same 10 mm NMR tube filled with 3 mL of 100 m_M Py that was hyperpolarized to (0.2 ± 0.02) % [hyperpolarization level and a signal enhancement of (0.95 ± 0.1) × 10^5 were evaluated by signal referencing to a sample of thermally polarized water; see Figure 4 b]. An earlier in situ low-field SABRE NMR spectroscopic study at about 5 mT reported a P_H of 0.05 % for approximately 300 m_M Py in a similar volume (≈ 4.3 mL),[19] and our results compare favorably in terms of the demonstrated polarization level. The SNR level (Figure 4 a), if compared to that in Figure 3 d, e, is certainly sufficient to enable in situ molecular imaging of dilute hyperpolarized compounds at such a relatively low magnetic field. Even lower magnetic fields can in principle be used for HP MRI[7a] to make studies more economical and less hardware demanding. For example, magnet power supply operating power can be reduced. Due to hardware limitations, imaging capabilities were not available to us at 5.75 mT. We also demonstrated that this relatively simple 5.75 mT NMR setup can monitor the buildup and decay of hyperpolarization dynamics (Figure 4 c), which was controlled by the initiation and cessation of *p*-H_2 bubbling. In this time series consisting of 128 NMR spectra, a single-scan ^{1}H NMR spectrum was acquired every 1 s with a small tipping angle RF excitation pulse (18° pulse preserving more than 95 % of the available proton *z* magnetization) immediately after the start of parahydrogen bubbling. *p*-H_2 bubbling was stopped before the NMR time series ended, which allowed the decay of the HP species to be monitored. Note that the time-resolved in situ NMR spectra of hyperpolarization buildup and decay (Figure 4 a, c) were denoised by using singular value decomposition (see the Experimental Section). Whereas the buildup and decay of SABRE hyperpolarization was demonstrated previously by Hövener and co-workers,[6d] it was performed by using 90° excitation pulses. The approach used in this study uses small-angle excitation RF pulses, which retain more than 95% of the available magnetization. As a result, the kinetics of the buildup and decay can be measured by using a single experiment of *p*-H_2 introduction and cessation. The determined value of the SABRE exponential buildup time constant [(7.4 ± 0.3) s] is similar to that reported previously (≈ 5.5 s).[19] Whereas time-resolved NMR spectroscopy was performed earlier with identical temporal resolution (1 s),[19] the use of 90° excitation pulses[19] did not allow the direct measurement of SABRE buildup and SABRE decay. Therefore, the data shown in Figure 4 c is the first report of the direct observation of SABRE buildup and decay detected in real time. Moreover, this time-resolved in situ spectroscopic study is useful, because it allows one to measure the effective buildup and decay of gas saturation in a gas–liquid exchange process during bubbling, which is hardly possible by using conventional high-field NMR due to line-shape distortions and broadening caused by susceptibility artifacts. Furthermore, this detection was performed in an approximately 0.7 L RF coil encompassing the entire sample (compared to a ≈0.5 mL RF coil of a conventional high-field NMR spectrometer, which usually records an NMR signal from a small fraction of the NMR sample). Finally, more advanced electromagnet-

based NMR systems have been used for NMR detection in a few-milli-Tesla regime.[6d, 7b, c, 19] These setups greatly benefited from more homogeneous magnet designs and significantly more stable power supplies. These desired advances can enable even more sensitive spectroscopic low-field NMR detection through NMR line narrowing due to more homogeneous B_0. These additional gains in NMR sensitivity can be used to enable high-resolution MRI and the detection of smaller quantities of hyperpolarized media.

3. Conclusions

To summarize, low-field NMR and MRI of dilute hyperpolarized (HP) compounds prepared by using the spin order of *p*-H_2 and the SABRE approach were demonstrated with high spatial and temporal resolution. In situ and ex situ modes of NMR and MRI were demonstrated at a magnetic field as low as 5.75 mT, which was generated by a relatively simple electromagnet. Ex situ MRI of a liquid solution after exchange with *p*-H_2 was successfully performed at 47.5 mT with sub-millimeter in-plane spatial resolution (pixel size 125 × 125 μm^2) in a few seconds; this demonstrated the feasibility of low-field parahydrogen-based hyperpolarization detection with ultra-high spatial and temporal resolution. Ultrafast 3D MRI of HP gases was demonstrated,[8b] and ultrafast 3D low-field MRI[24] can in principle be applied to SABRE hyperpolarized contrast agents leading to 3D MRI images with sub-millimeter voxel size, because sufficient NMR sensitivity was already demonstrated, as seen in Figure 3 e with an effective voxel size of <0.5 mm^3. Furthermore, in situ low-field NMR and MRI were also employed for imaging of the product (pyridine) and intermediates (iridium dihydride) of hydrogen exchange during hydrogen gas bubbling though the solution. Time-resolved NMR spectra were detected with a high signal-to-noise ratio by using an approximately 0.7 L NMR coil at relatively low concentrations of HP compounds and relatively low NMR hyperpolarization levels of < 1%. Nevertheless, 2D projection MRI with sub-millimeter in-plane resolution (i.e. < 1 mm^2) was achieved even in the case of sample phase heterogeneity, as demonstrated by imaging of Py solution during *p*-H_2 bubbling.

Low-field NMR and MRI may be useful to visualize the distribution of chemical species inside industrial reactors based on their different NMR properties: chemical shift difference (e.g. pyridine and Ir–dihydride) and field-dependent hyperpolarization behavior. Although the presented results are system specific, there are no fundamental limitations to exploit SABRE-based hyperpolarization (including other substrates, heterogeneous SABRE and SABRE in water) for low-field chemical magnetic resonance imaging. Low-field NMR/MRI setups are simple, inexpensive, and do not demand cryogenically cooled superconducting magnets and, therefore, are suitable for low-cost and large-scale imaging applications.

Experimental Section

Low-Field Ex Situ and In Situ NMR Spectroscopy at 47.5 mT

Hydrogen gas enriched with the *para*-spin isomer to the value of ≥ 90% was created by using a previously described *p*-H_2 generator.[29] *p*-H_2 was bubbled through a 1.6 mm OD [0.8 mm inner diameter (ID) polytetrafluoroethylene (PTFE) tubing (McMaster-Carr, Atlanta, GA, USA p/n 5239K23) placed inside a 5 mm OD medium-walled NMR tube filled

with about 0.75 mL of a 100 mM Py and 7 mM [IrCl(cod)(IMes)] catalyst [IMes=1,3-bis(2,4,6-trimethylphenyl)imidazol-2-ylidene; cod=cyclooctadiene][11b, 30] solution in CD_3OD (Isotec-Sigma–Aldrich). Then, two different experimental protocols were exploited for NMR acquisition by using a frequency-optimized dual channel RF coil reported earlier with a ^{1}H-X configuration.[7a] In the first protocol, *p*-H_2 bubbling and signal detection were performed at the same magnetic field of 47.5 mT (Figure 1 a), which corresponded to the conditions of in situ MR detection. In the second protocol, *p*-H_2 bubbling was performed in a 5.75 mT magnet, then stopped, and was followed by rapid transfer of the sample tube assembly (<8 s) to a 47.5 mT magnet for detection (e.g. Figure 1 b). NMR proton signal enhancement (ε) was calculated by comparing the NMR signal integral values derived from the NMR spectra of a HP sample and the corresponding thermally polarized sample of Py with known proton nuclear spin polarization ($P_H = 1.6 \times 10^{-7}$ at 47.5 mT and 25°C) according to Equation (1):

$$\varepsilon = \left(\frac{S_{HP}}{S_{REF}}\right) \times \left(\frac{C_{REF}}{C_{HP}}\right) \times \left(\frac{NH_{REF}}{NH_{HP}}\right) \times \left(\frac{\sin(\alpha_{REF})}{\sin(\alpha_{HP})}\right) \times \left(\frac{A_{REF}}{A_{HP}}\right) \quad (1)$$

in which S_{HP} and S_{REF} are the integral values over the spectral region for HP and thermally polarized reference samples, respectively; C_{HP} and C_{REF} are the molar concentrations of HP and thermally polarized reference samples, respectively; NH_{HP} and NH_{REF} are the number of protons per each molecule in HP and thermal reference samples, respectively; α_{HP} and α_{REF} are the RF excitation pulse tipping angles used for NMR detection of signals in HP and thermal reference samples, respectively; and A_{REF} and A_{HP} are the effective cross sections (i.e. inner area) of the NMR tubes for reference and HP samples. Hyperpolarization of Py was performed in a 3.43 mm ID NMR tube (medium wall) with 1.6 mm OD PTFE tubing inserted inside for *p*-H_2 bubbling. A single-scan reference spectrum for thermally polarized Py was acquired in a completely filled 4.14 mm (ID) NMR tube. Notably, during NMR signal detection in the 47.5 mT NMR system the effective sample length that contributed to the NMR signal was about 80 mm. Concentration of neat Py (12.4 M) in the thermally polarized sample was around 124 times greater than that in a given HP sample (0.1 M). The ratio of (S_{HP}/S_{REF}) was roughly 78. The ratio (A_{REF}/A_{HP}), was about 1.85. A 90° RF pulse angle was used for detection of the thermally polarized reference spectrum (Figure 2 c), whereas a 10° excitation RF pulse was used for HP detection (Figure 2 a, b), which resulted in a $\sin(\alpha_{REF})/\sin(\alpha_{HP})$ ratio of about 5.8. Therefore, the ex situ NMR signal enhancement of Py was found to be $\varepsilon = (1 \pm 0.1) \times 10^5$, which corresponds to a nuclear spin polarization of $P_H = (1.6 \pm 0.16)$ %.

Low-Field Ex Situ and In Situ MRI at 47.5 mT

Low-field ex situ and in situ MRI at 47.5 mT were performed by using an approximately 3 mL sample of a separate batch of Py/Ir-catalyst solution in CD_3OD (as described above) placed inside a 10 mm OD NMR tube. A 1.6 mm OD capillary was used for *p*-H_2 bubbling through this solution. The following imaging parameters were used for in situ 2D MRI (Figure 3 d) by using the gradient echo sequence supplied by the equipment manufacturer (Magritek, Wellington, New Zealand) during *p*-H_2 bubbling: acquisition time = 6.4 ms, echo time (TE) = 7 ms, repetition time (TR) = 200 ms, field of view (FOV) = 96 × 96 mm^2,

spectral width (SW) = 20 kHz, imaging matrix = 128 × 128, RF pulse of 15 μs (α = 15°), number of averages (NA) = 32, 33 % of *k*-space sampling (under-sampling did not induce any visible imaging artifacts but reduced the total imaging time significantly),[18] which resulted in effective spatial and temporal resolutions of 0.75 × 0.75 mm^2 and 4.5 min, respectively. The following imaging parameters were used for ex situ 2D MRI (Figure 3 e, top) by using the gradient echo sequence after sample transfer into the 47.5 mT MRI system: acquisition time = 12.8 ms, TE = 13 ms, TR = 60 ms, FOV = 32 × 32 mm^2, SW = 20 kHz, imaging matrix = 256 × 256, RF pulse of 10 μs (α = 9°), NA = 1, 50% of *k*-space sampling resulting in effective spatial and temporal resolutions of 0.125 × 0.125 mm^2 and 7.7 s. The imaging parameters for the image shown in Figure 3 e (bottom) were: acquisition time = 25.6 ms, TE = 26 ms, TR = 60 ms, FOV = 64 × 64 mm^2, SW = 20 kHz, imaging matrix = 512 × 512, RF pulse of 10 μs (α = 9°), NA = 1, 20% of *k*-space sampling resulting in effective spatial and temporal resolutions of 0.125 × 0.125 mm^2 and about 6 s, respectively.

Low-Field In Situ NMR Spectroscopy at 5.75 mT

Low-field NMR hyperpolarizers for PHIP have utilized electromagnets with a solenoid design.[31] Although more sophisticated NMR electromagnet designs[7c, 19, 32] were recently demonstrated, including those for PHIP and SABRE detection,[6d, 33] this work utilized a relatively simple NMR electromagnet design described earlier.[18] NMR spectroscopy was performed by using a dual channel RF PHIP probe by using a previous design[34] with 1) an inner solenoid that was replaced by a 51 mm ID saddle-shape RF coil, and 2) the probe channels were tuned to 244 kHz (outer coil) and 62 kHz (inner coil) through modification of the RF circuit. The overall PHIP hyperpolarizer setup was used previously,[35] in which the high-pressure reactor was removed for access to the 51 mm ID bore of the RF coil. NMR spectra were recorded at 244 kHz resonance frequency by using an approximately 0.7 L saddle-shape RF coil. All NMR spectra were recorded by using a 3 mL sample of the Ir-IMes catalyst and Py described above and placed inside a 10 mm (OD) NMR tube. The proton NMR signal enhancement (ε) was calculated by comparison of the NMR signal integral values derived from the NMR spectra of the HP sample and the thermally polarized sample of Py with known proton nuclear spin polarization (P_H=2.0 × 10^{-8} at 5.75 mT and 25 °C) according to Equation (2):

$$\varepsilon = \left(\frac{S_{\mathrm{HP}}}{S_{\mathrm{REF}}}\right) \times \left(\frac{\chi_{\mathrm{REF}}}{\chi_{\mathrm{HP}}}\right) \times \left(\frac{NH_{\mathrm{REF}}}{NH_{\mathrm{HP}}}\right) \times \left(\frac{\sin(\alpha_{\mathrm{REF}})}{\sin(\alpha_{\mathrm{HP}})}\right) \quad (2)$$

in which S_{HP} and S_{REF} are the integral values over the spectral region for the HP and the thermally polarized reference samples, respectively; χ_{HP} and χ_{REF} are the molar quantities (in moles) of the HP and the thermally polarized reference samples, respectively; NH_{HP} and NH_{REF} are the number of protons per each molecule in the HP and the thermal reference samples, respectively; and α_{HP} and α_{REF} are the RF excitation pulse angles used for NMR detection of signals in the HP and the thermal reference samples, respectively. A signal from a reference sample of water phantom (17.5 mL) was used. Thus, the molar ratio between the total amount of water and Py was 3.2 × 10^3. The ratio of (S_{HP}/S_{REF}) was about 22.7. An RF pulse with a 90° flip angle was used to record the thermally polarized spectrum (Figure 4 a), whereas an 18° excitation RF pulse was used for HP detection (Figure 4 b), which resulted

in a $\sin(\alpha_{REF})/\sin(\alpha_{HP})$ ratio of roughly 3.2. The NH_{REF}/NH_{HP} ratio was 0.4 owing to the presence of five protons in Py and two protons in H_2O. Therefore, the in situ NMR signal enhancement of Py was calculated to be $\varepsilon = (0.95 \pm 0.1) \times 10^5$, which corresponds to a nuclear spin polarization of $P_H = (0.2 \pm 0.02)$ %. Singular value decomposition was used for de-noising the data obtained in the time-resolved in situ NMR detection of hyperpolarization buildup and decay (Figure 4 a, c) by taking advantage of random noise in all 128 NMR spectra outside of the NMR peak region. Data matrix **M** for the set of recorded spectra was constructed in a manner for which each column was the data for a single experiment with the length n and the number of columns was the number of experiments, m (in our case m = 128). The singular value decomposition of matrix ($M = U \sum V^{\dagger}$) was performed by using Matlab software. Therein, **U** [$n \times n$] was a matrix of left singular vectors, **V** [$m \times m$] was a matrix of right singular vectors, and $\sum[n \times m]$ was a diagonal matrix with positive real singular values along the diagonal. Small singular values are known to be associated with random noise; hence, near-zero singular values were removed and a new data matrix was reconstructed.[36] The presented data was reconstructed by using only the first six maximum singular values, which improved the SNR by at least a factor of five.

Supplementary Material

Refer to Web version on PubMed Central for supplementary material.

Acknowledgements

D.A.B., K.V.K., and I.V.K. thank the Russian Science Foundation (grant 14–13–00445) for support of the ex situ SABRE experiments. E.Y.C. thanks the National Institutes of Health (NIH) (5R00 CA134749–03, 3R00 A134749–02S1) for funding support and the DoD Congressionally Directed Medical Research Programs Breast Cancer Program Era of Hope Award (W81XWH-12–1–0159/BC112431) for support in performing the MRI and NMR experiments. This material is based upon work supported by the National Science Foundation under CHE—1416268. The reported study was partially supported by Russian Foundation for Basic Research, research project No. 14-03-93183 MCX a. B.M.G. is a member of the SIUC Materials Technology Center.

References

1. a) Ernst RR. Angew. Chem. Int. Ed. Engl. 1992; 31:805–823. *Angew. Chem.***1992**, *104*, 817 – 836. b) Lauterbur PC. Nature. 1973; 242:190–191.
2. a) Levitt, MH. Spin Dynamics: Basics of Nuclear Magnetic Resonance. Chichester: Wiley; 2008. b) Keeler, J. Understanding NMR Spectroscopy. Chichester: Wiley; 2013.
3. a) Koptyug IV. Prog. Nucl. Magn. Reson. Spectrosc. 2012; 65:1–65. [PubMed: 22781314] b) Bonhomme C, Gervais C, Laurencin D. Prog. Nucl. Magn. Reson. Spectrosc. 2014; 77:1–48. [PubMed: 24411829] c) Van As H, van Duynhoven J. J. Magn. Reson. 2013; 229:25–34. [PubMed: 23369439]
4. a) Dalitz F, Cudaj M, Maiwald M, Guthausen G. Prog. Nucl. Magn. Reson. Spectrosc. 2012; 60:52–70. [PubMed: 22293399] b) Zalesskiy SS, Danieli E, Blümich B, Ananikov VP. Chem. Rev. 2014; 114:5641–5694. [PubMed: 24779750] c) Mitchell J, Gladden LF, Chandrasekera TC, Fordham EJ. Prog. Nucl. Magn. Reson. Spectrosc. 2014; 76:1–60. [PubMed: 24360243]
5. Tsai LL, Mair RW, Rosen MS, Patz S, Walsworth RL. J. Magn. Reson. 2008; 193:274–285. [PubMed: 18550402]
6. a) Nikolaou P, Coffey AM, Barlow MJ, Rosen MS, Goodson BM, Chekmenev EY. Anal. Chem. 2014; 86:8206–8212. [PubMed: 25008290] b) Dominguez-Viqueira W, Parra-Robles J, Fox M, Handler WB, Chronik BA, Santyr GE. Concept Magnetic Res. B. 2008; 33B:124–137.c) Glöggler S, Muller R, Colell J, Emondts M, Dabrowski M, Blumich B, Appelt S. Phys. Chem. Chem. Phys. 2011; 13:13759–13764. [PubMed: 21720644] d) Borowiak R, Schwaderlapp N, Huethe F, Lickert

T, Fischer E, Bär S, Hennig J, Elverfeldt D, Hövener J-B. Magn. Reson. Mater. Phys. 2013; 26:491–499.e) Ruset IC, Tsai LL, Mair RW, Patz S, Hrovat MI, Rosen MS, Muradian I, Ng J, Topulos GP, Butler JP, Walsworth RL, Hersman FW. Concept Magnetic Res. B. 2006; 29B:210–221.f) Venkatesh AK, Zhang AX, Mansour J, Kubatina L, Oh CH, Blasche G, Unlu MS, Balamore D, Jolesz FA, Goldberg BB, Albert MS. Magn. Reson. Imaging. 2003; 21:773–776. [PubMed: 14559342]

7. a) Coffey AM, Truong ML, Chekmenev EY. J. Magn. Reson. 2013; 237:169–174. [PubMed: 24239701] b) Appelt S, Kuhn H, Hasing FW, Blumich B. Nature Phys. 2006; 2:105–109.c) Blümich B, Casanova F, Appelt S. Chem. Phys. Lett. 2009; 477:231–240.
8. a) Nikolaou P, Coffey AM, Walkup LL, Gust BM, LaPierre CD, Koehnemann E, Barlow MJ, Rosen MS, Goodson BM, Chekmenev EY. J. Am. Chem. Soc. 2014; 136:1636–1642. [PubMed: 24400919] b) Nikolaou P, Coffey AM, Walkup LL, Gust BM, Whiting N, Newton H, Barcus S, Muradyan I, Dabaghyan M, Moroz GD, Rosen MS, Patz S, Barlow MJ, Chekmenev EY, Goodson BM. Proc. Natl. Acad. Sci. USA. 2013; 110:14150–14155. [PubMed: 23946420] c) Goodson BM. J. Magn. Reson. 2002; 155:157–216. [PubMed: 12036331] d) Walker TG, Happer W. Rev. Mod. Phys. 1997; 69:629–642.e) Nelson IA, Chann B, Walker TG. Appl. Phys. Lett. 2000; 76:1356–1358.f) Walker TG. J. Phys. Conf. Ser. 2011; 294:012001.
9. a) Maly T, Debelouchina GT, Bajaj VS, Hu KN, Joo CG, Mak-Jurkauskas ML, Sirigiri JR, van der Wel PCA, Herzfeld J, Temkin RJ, Griffin RG. J. Chem. Phys. 2008; 128:052211. [PubMed: 18266416] b) Koptyug IV. Mendeleev Commun. 2013; 23:299–312.c) Abragam A, Goldman M. Rep. Prog. Phys. 1978; 41:395.
10. a) Natterer J, Bargon J. Prog. Nucl. Magn. Reson. Spectrosc. 1997; 31:293–315.b) Bowers CR, Weitekamp DP. J. Am. Chem. Soc. 1987; 109:5541–5542.c) Pravica MG, Weitekamp DP. Chem. Phys. Lett. 1988; 145:255–258.
11. a) Adams RW, Aguilar JA, Atkinson KD, Cowley MJ, Elliott PIP, Duckett SB, Green GGR, Khazal IG, Lopez-Serrano J, Williamson DC. Science. 2009; 323:1708–1711. [PubMed: 19325111] b) Cowley MJ, Adams RW, Atkinson KD, Cockett MCR, Duckett SB, Green GGR, Lohman JAB, Kerssebaum R, Kilgour D, Mewis RE. J. Am. Chem. Soc. 2011; 133:6134–6137. [PubMed: 21469642]
12. Atkinson KD, Cowley MJ, Elliott PIP, Duckett SB, Green GGR, Lopez-Serrano J, Whitwood AC. J. Am. Chem. Soc. 2009; 131:13362–13368. [PubMed: 19719167]
13. Shi F, Coffey AM, Waddell KW, Chekmenev EY, Goodson BM. Angew. Chem. Int. Ed. 2014; 53:7495–7498. *Angew. Chem.***2014**, *126*, 7625 – 7628.
14. a) Zeng H, Xu J, McMahon MT, Lohman JA, van Zijl P. J. Magn. Reson. 2014; 246:119–121. [PubMed: 25123540] b) Hövener JB, Schwaderlapp N, Borowiak R, Lickert T, Duckett SB, Mewis RE, Adams RW, Burns MJ, Highton LAR, Green GGR, Olaru A, Hennig J, von Elverfeldtt D. Anal. Chem. 2014; 86:1767–1774. [PubMed: 24397559] c) Truong ML, Shi F, He P, Yuan B, Plunkett KN, Coffey AM, Shchepin RV, Barskiy DA, Kovtunov KV, Koptyug IV, Waddell KW, Goodson BM, Chekmenev EY. unpublished results.
15. Adams RW, Duckett SB, Green RA, Williamson DC, Green GGR. J. Chem. Phys. 2009; 131:194505. [PubMed: 19929058]
16. Barskiy DA, Kovtunov KV, Koptyug IV, He P, Groome KA, Best QA, Shi F, Goodson BM, Shchepin RV, Coffey AM, Waddell KW, Chekmenev EY. J. Am. Chem. Soc. 2014; 136:3322–3325. [PubMed: 24528143]
17. a) Waddell KW, Coffey AM, Chekmenev EY. J. Am. Chem. Soc. 2011; 133:97–101. [PubMed: 21141960] b) Bouchard LS, Burt SR, Anwar MS, Kovtunov KV, Koptyug IV, Pines A. Science. 2008; 319:442–445. [PubMed: 18218891] c) Telkki VV, Zhivonitko VV, Ahola S, Kovtunov KV, Jokisaari J, Koptyug IV. Angew. Chem. Int. Ed. 2010; 49:8363–8366. *Angew. Chem.***2010**, *122*, 8541 – 8544. d) Zhivonitko VV, Telkki VV, Leppaniemi J, Scotti G, Franssila S, Koptyug IV. Lab Chip. 2013; 13:1554–1561. [PubMed: 23435499]
18. Coffey AM, Kovtunov KV, Barskiy D, Koptyug IV, Shchepin RV, Waddell KW, He P, Groome KA, Best QA, Shi F, Goodson BM, Chekmenev EY. Anal. Chem. 2014; 86:9042–9049. [PubMed: 25162371]

19. Hövener JB, Schwaderlapp N, Lickert T, Duckett SB, Mewis RE, Highton LAR, Kenny SM, Green GGR, Leibfritz D, Korvink JG, Hennig J, von Elverfeldt D. Nat. Commun. 2013; 4:2946. [PubMed: 24336292]
20. Hövener JB, Knecht S, Schwaderlapp N, Hennig J, von Elverfeldt D. Chem Phys Chem. 2014; 15:2451–2457. [PubMed: 25079961]
21. Eshuis N, Hermkens N, van Weerdenburg BJA, Feiters MC, Rutjes F, Wijmenga SS, Tessari M. J. Am. Chem. Soc. 2014; 136:2695–2698. [PubMed: 24475903]
22. Dücker EB, Kuhn LT, Munnemann K, Griesinger C. J. Magn. Reson. 2012; 214:159–165. [PubMed: 22153915]
23. Kobayashi J, Mori Y, Okamoto K, Akiyama R, Ueno M, Kitamori T, Kobayashi S. Science. 2004; 304:1305–1308. [PubMed: 15166375]
24. Sarracanie M, Armstrong BD, Stockmann J, Rosen MS. Magn. Reson. Med. 2014; 71:735–745.
25. Zeng HF, Xu JD, Gillen J, McMahon MT, Artemov D, Tyburn JM, Lohman JAB, Mewis RE, Atkinson KD, Green GGR, Duckett SB, van Zijl PCM. J. Magn. Reson. 2013; 237:73–78. [PubMed: 24140625]
26. Tayler MCD, Levitt MH. Phys. Chem. Chem. Phys. 2011; 13:5556–5560. [PubMed: 21318206]
27. DeVlence SJ, Walsworth RL, Rosen MS. Phys. Rev. Lett. 2013; 111:173002. [PubMed: 24206484]
28. Pileio G, Carravetta M, Hughes E, Levitt MH. J. Am. Chem. Soc. 2008; 130:12582–12583. [PubMed: 18729363]
29. Feng BB, Coffey AM, Colon RD, Chekmenev EY, Waddell KW. J. Magn. Reson. 2012; 214:258–262. [PubMed: 22188975]
30. Vazquez-Serrano LD, Owens BT, Buriak JM. Inorg. Chim. Acta. 2006; 359:2786–2797.
31. a) Hövener J-B, Chekmenev E, Harris K, Perman W, Robertson L, Ross B, Bhattacharya P. Magn. Reson. Mater. Phys. 2009; 22:111–121.b) Kadlecek S, Vahdat V, Nakayama T, Ng D, Emami K, Rizi R. NMR Biomed. 2011; 24:933–942. [PubMed: 21845739]
32. Appelt S, Gloggler S, Hasing FW, Sieling U, Nejad AG, Blumich B. Chem. Phys. Lett. 2010; 485:217–220.
33. Türschmann P, Colell J, Theis T, Blumich B, Appelt S. Phys. Chem. Chem. Phys. 2014; 16:15411–15421. [PubMed: 24947652]
34. Coffey AM, Shchepin RV, Wilkens K, Waddell KW, Chekmenev EY. J. Magn. Reson. 2012; 220:94–101. [PubMed: 22706029]
35. Shchepin RV, Coffey AM, Waddell KW, Chekmenev EY. Anal. Chem. 2014; 86:5601–5605. [PubMed: 24738968]
36. De Lathauwer L, De Moor B, Vandewalle J. SIAM J. Matrix Anal. Appl. 2000; 21:1253–1278.

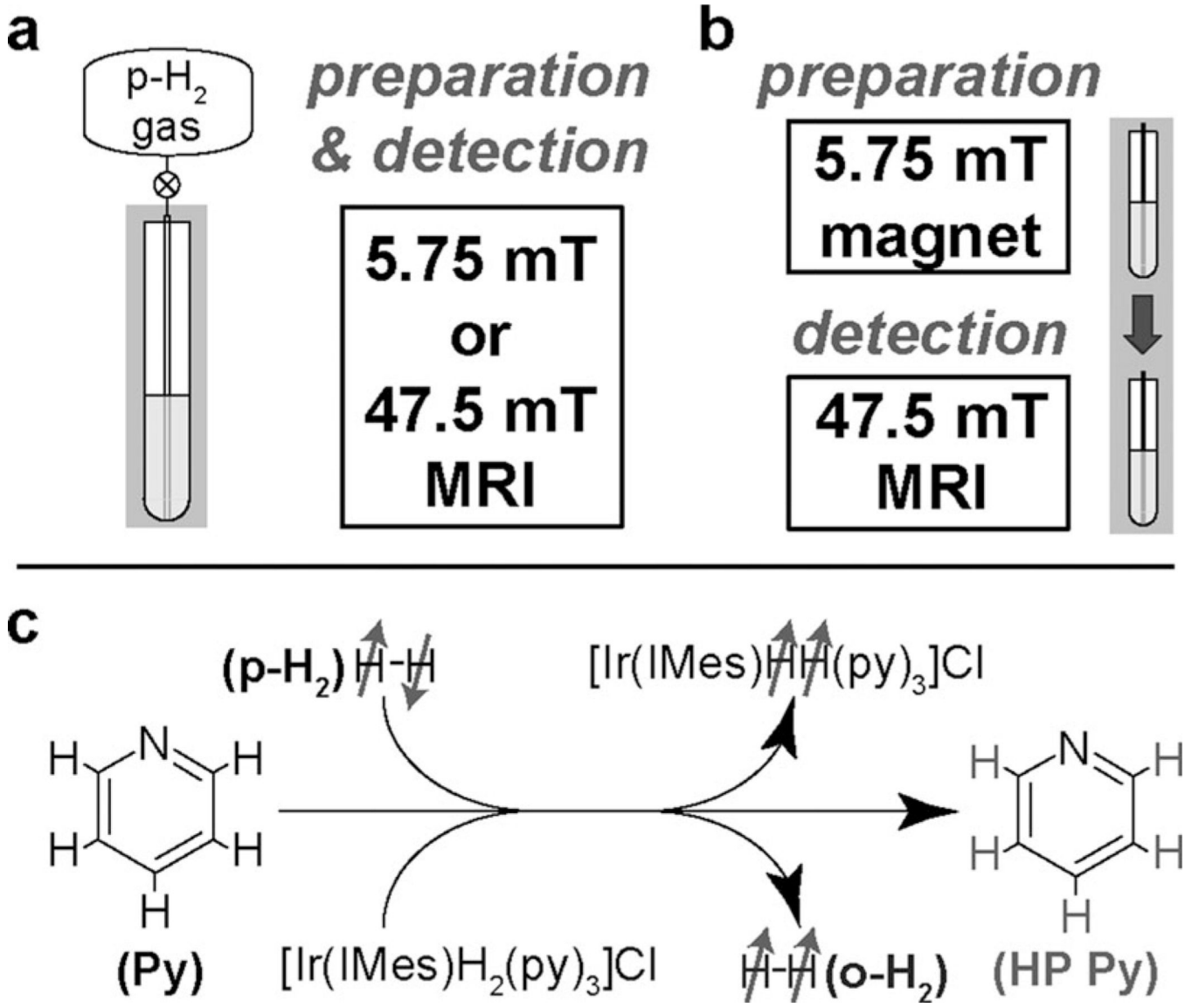

Figure 1.

Schematic diagram of the experimental setup for ^{1}H NMR/MRI at low magnetic fields: a) In situ detection for which preparation (chemical exchange/polarization transfer) and detection were both performed in the same magnetic field (5.75 or 47.5 mT). b) Ex situ detection for which preparation (chemical exchange/polarization transfer) was performed at 5.75 mT and was followed by rapid transfer (≈ 8 s) to a 47.5 mT field for detection. Note that the ex situ approach primarily detects only one HP product (pyridine), whereas in situ detection allows "capturing" the HP product (pyridine) and two HP intermediates/byproducts (Ir–dihydride and orthohydrogen). No additional magnetic field (except that provided by Earth) was used during transfer of the sample from the 5.75 to 47.5 mT magnet for ex situ experiments. c) Molecular diagram of the exchange process between gaseous parahydrogen, the Ir complex, and pyridine to lead to the polarization transfer from parahydrogen (p-H_2) to pyridine (Py), Ir–dihydride, and orthohydrogen (o-H_2).

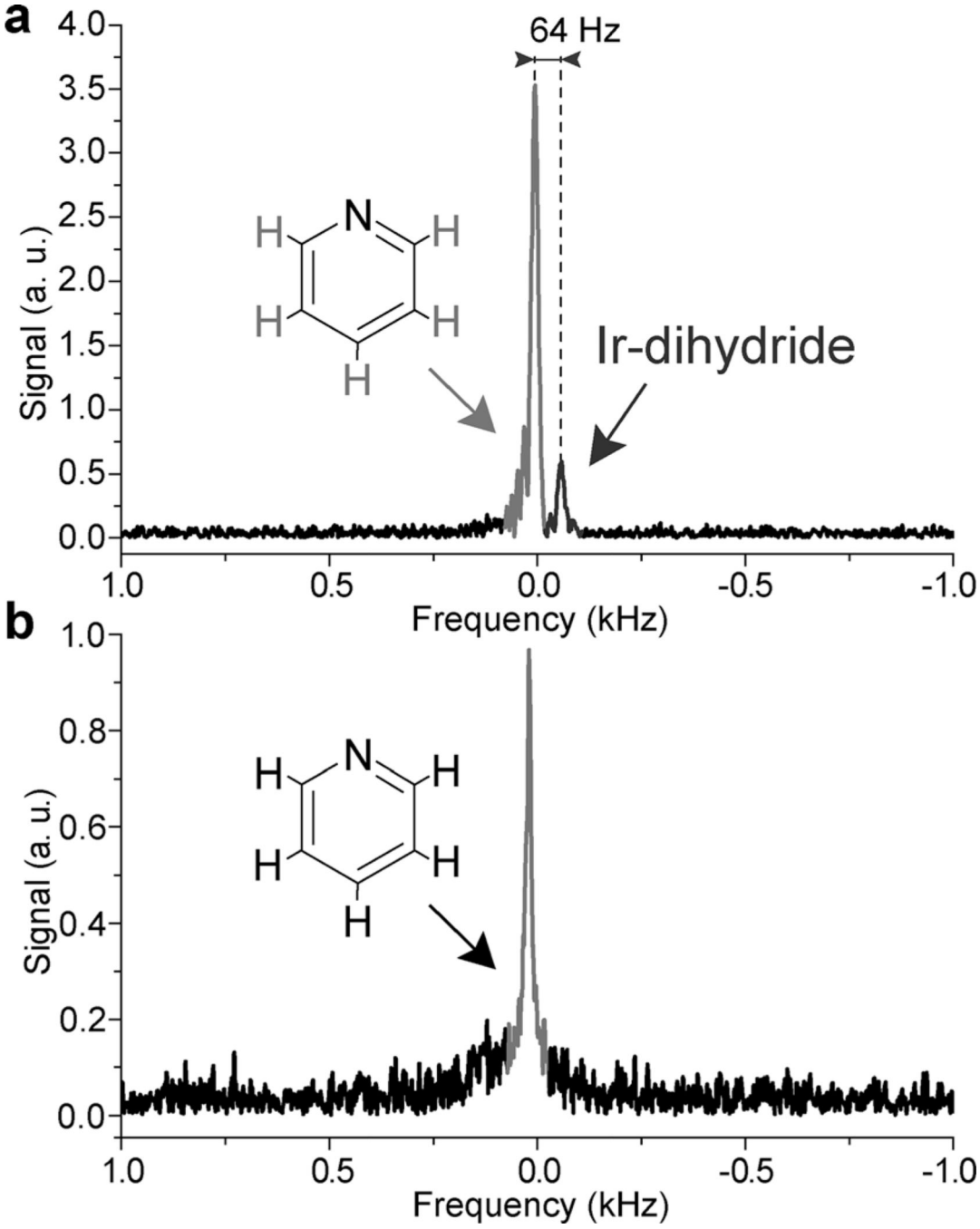

Figure 2.

Single-scan proton NMR spectra (magnitude mode spectra) of SABRE hyperpolarization of a 100 mM pyridine (Py) solution in [D_4]MeOH. a) In situ detection of SABRE hyperpolarization during *p*-H_2 bubbling at 47.5 mT (preparation and detection). Note the characteristic chemical shift difference of 64 Hz corresponding to a difference of 31.5 ppm between the signals for HP Py (and *o*-H_2) and Ir–dihydride. b) Reference ^{1}H NMR spectrum of neat (12.4 M) Py at 47.5 mT. The spectra were recorded in medium walled (a) and standard (b) 5 mm NMR tubes with a FWHH of 19.5 and 17.6 Hz, respectively. Note the

direction of the resonance frequency axis indicating that Ir–dihydride protons resonate at lower Larmor frequency.

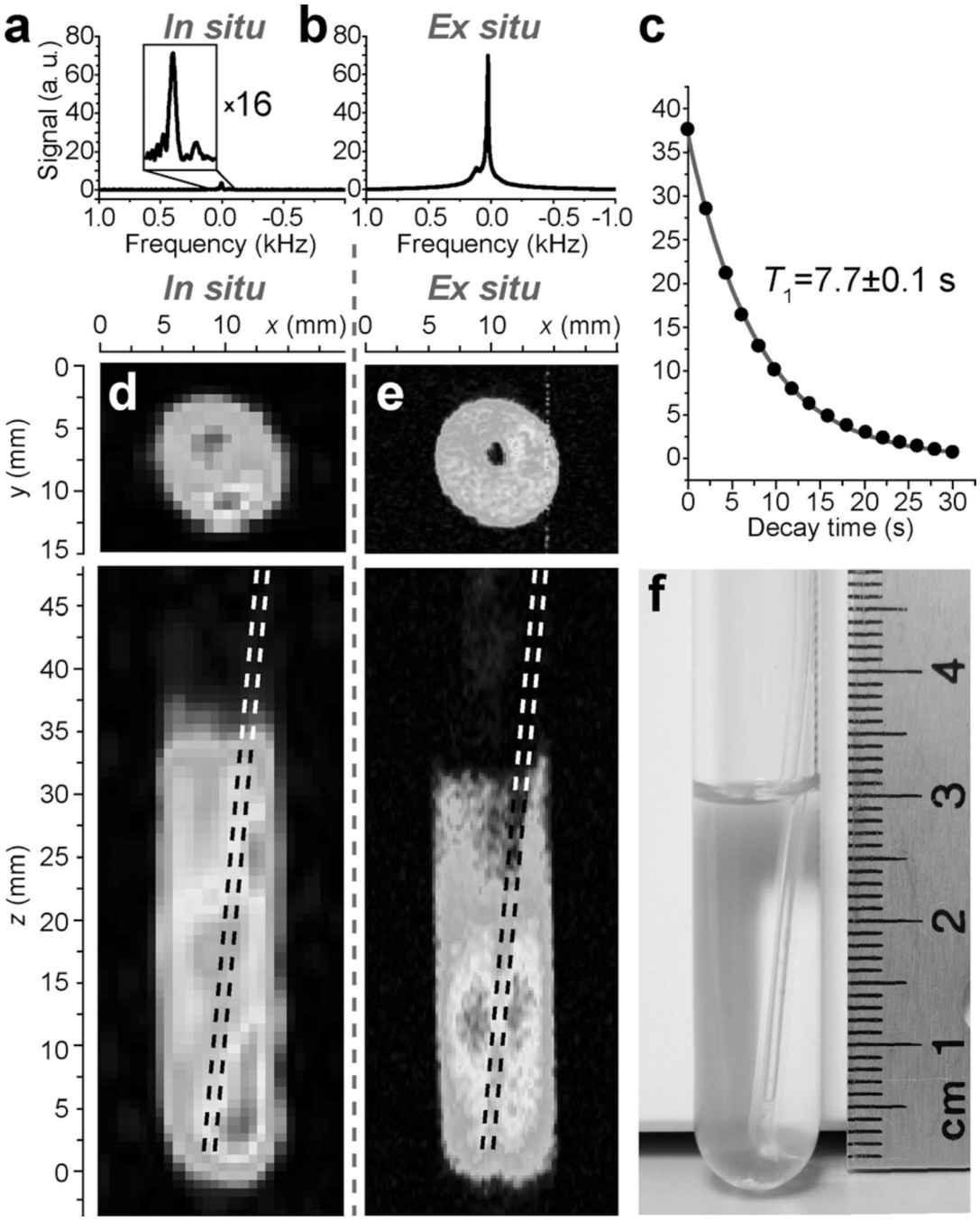

Figure 3.

a) NMR spectrum of in situ SABRE hyperpolarization during *p*-H_2 bubbling at 47.5 mT. b) NMR spectrum of ex situ SABRE hyperpolarization with preparation at 5.75 mT and subsequent detection at 47.5 mT after about an 8 s long transfer delay. c) Ex situ T_1 decay of HP Py detected with 10° excitation RF pulse at 47.5 mT. The simulation (gray line) used the mono-exponential decay function $y = A \times \exp(-x/T_1)$. d) Two orthogonal projections of non-slice-selective MRI of in situ SABRE detection at 47.5 mT with digital resolution (in-plane pixel size) of 0.75 × 0.75 mm^2 and effective voxel size (defined as the product of pixel size

and sample depth) of < 16 mm^3. e) Two orthogonal projections of non-slice-selective MRI of ex situ SABRE of Py with digital resolution (in-plane pixel size) of 0.125 × 0.125 mm^2 and effective voxel size (defined as the product of pixel size and sample depth) of < 0.5 mm^3. f) Photograph of an approximately 3 mL solution of 100 mM Py with 7 mM Ir catalyst in a 10 mm NMR tube with 1.6 mm OD PTFE tubing for parahydrogen bubbling at 1 atm. Note the partial solvent ($[D_4]$MeOH) loss in the image given in e) due to evaporation by *p*-H_2 bubbling. The inner hole in the upper images is due to the 1.6 mm OD PTFE tubing used for delivery of *p*-H_2 gas. For additional details, see the color version of this and all other figures in Supporting Information.

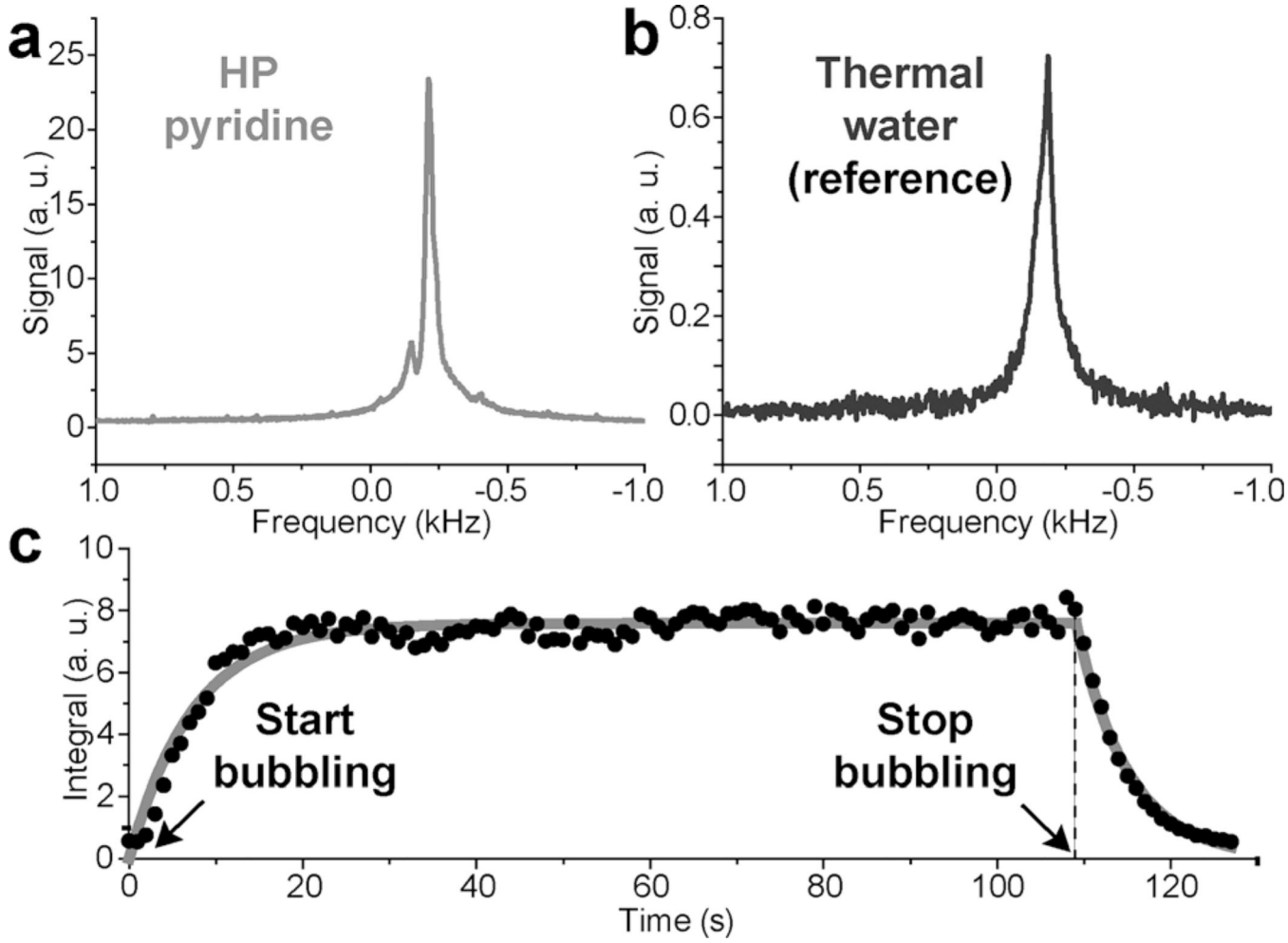

Figure 4.

In situ NMR spectra at 5.75 mT. a) Magnitude ^{1}H NMR spectrum of SABRE HP Py sample during *p*-H_2 bubbling. b) Magnitude ^{1}H NMR spectrum of the water reference sample recorded by using 256 averages. c) Time-resolved (1 s temporal resolution) in situ monitoring of SABRE signal buildup and decay by using single-scan NMR detection and a 18° RF excitation pulse. Single monoexponential decay and growth functions were used for fitting to yield a fitted T_1 signal decay curve corresponding to the buildup (after *p*-H_2 bubbling was started) time constant of (7.4 ± 0.3) s, and effective T_1 decay constant of (5.6 ± 0.1) s (after *p*-H_2 bubbling was stopped).